Stabilizing Fe single atom catalysts by implanting Cr atomic clusters to boost oxygen reduction reaction

Yingying Guo, Chenhui Wang, Yuhang Xiao, Xiaohong Tan, Weidong He, Jianpo Chen, Yan Li, Hao Cui [*], Chengxin Wang [*]

School of Materials Science and Engineering, Sun Yat-sen University, Guangzhou 510275, China

ARTICLE INFO

ABSTRACT

Fe single-atom catalysts (SACs) have emerged as a promising alternative to platinum for catalyzing oxygen reduction reactions (ORR). Nevertheless, their practical applicability is hindered by insufficient stability caused by structural corrosion during ORR. Here, we developed an effective strategy to optimize and stabilize the Fe SAs (single-atoms) sites by implanting chromium (Cr) atomic clusters (ACs) to address the formidable deactivation issue of the best-performing yet unstable Fe-N-C catalysts. Cr_{AC}-Fe_1/N-S-C demonstrates an amazing stability with a negligible decline in activity after 100,000 CV cycles, and can maintain 81% of initial current after a continuous 50-hour operation period. Theoretical calculations and experimental evidence substantiate that the integration of Cr ACs not only weakens the binding of OH* to the Fe site, thereby facilitating the ORR process, but also eliminates in situ-generated reactive oxygen species (ROS) and retards Fe ion leaching from active sites, thus stabilizing of the Fe SA sites.

1. Introduction

The enhancement of the oxygen reduction reaction (ORR) through the creation of electrocatalysts that are both exceptionally stable and highly active is of utmost importance in the progress of fuel cell and zinc-air battery applications [1–4]. Nevertheless, the insufficiency in the ORR efficiency of the majority of electrocatalysts persists due to the high level of energy demand necessary to disrupt the O═O bond, as well as the sluggish kinetics accompanying the $4e^-/4 H^+$ transfer process [5–8]. Recently, Fe-N-C single atom catalysts (SACs) with their remarkable properties of high atom utilization and high catalytic activity have shown remarkable potential in catalyzing electrochemical reactions [9–11]. Numerous researchers are engaged in the pursuit of enhancing the intrinsic activity of Fe SACs for ORR performance. This is accomplished by disrupting the symmetrical distribution of electron structures within Fe-N_4 molecules through the introduction of heteroatoms [12, 13], adjacent metal sites [14–17], and the intentional design of local defects [18–20], and so on. These strategies aim to facilitate the redistribution of electrons at the metal center atoms, consequently modifying the charge density of the metal centers and the adsorption characteristics of crucial intermediates. Significant research efforts have concentrated on ways to improve the intrinsic ORR activity of Fe SACs, with

comparatively fewer reports specifically addressing the improvement of their ORR stability. This discrepancy highlights the ongoing challenge of achieving both high intrinsic activity and long-term stability of Fe SACs.

Many Fe SAC catalysts still suffer obvious activity decrease after performing 5000–30000 CV cycles [21–25]. A fundamental comprehension of the degradation mechanisms impacting the stability of Fe-N-C catalysts is currently in progress. Due to the rapid commercial development of PEMFC, researchers predominantly focus on enhancing the stability of ORR in acidic media. Nevertheless, it is imperative to acknowledge that the stability of Fe-N-C in alkaline media falls short of practical requirements, and investigations in this realm are significantly limited. The degradation mechanisms associated with alkaline ORR are complex. In alkaline media, similar to acidic conditions, the Fe center can catalyze the formation of reactive oxygen species (ROS) from H_2O_2 (Fenton reaction), a by-product of the two-electron ORR [26–29]. The aggressive ROS generated, especially hydroxyl radicals (·OH), irreversibly destroy the carbon matrix of catalysts and the polymer membrane in PEMFCs. The attack of ROS on the catalyst has been proposed as the primary reason for the decay of ORR stability in acidic conditions. In addition, Fe ions will inevitably leach from the active sites during the ORR process, which is a non-negligible factor for activity decay in alkaline environments and is the major degradation mechanism in

---

* Corresponding authors.
  E-mail addresses: cuihao3@mail.sysu.edu.cn (H. Cui), wchengx@mail.sysu.edu.cn (C. Wang).

alkaline media. The dissolution of Fe from FeN_xC_y sites can be attributed to the instability of the coordinated Fe during the Fe^{3+}/Fe^{2+} redox transition. Therefore, it is crucial to eliminate *in situ*-generated ROS and retard Fe ion leaching from active sites to achieve excellent ORR catalysts. More recently, the introduction of another species has been found to be an effective means of modulating the electronic structure of the monatomic core and thus enhancing its interaction with the support, which also provides an idea for optimizing and stabilizing Fe SAs [30, 31]. The metal Cr possesses a distinctive outer electronic configuration of $3d^5 4s^1$. This configuration not only weakens the interaction between Cr^{2+}/Cr^{3+} ions and H_2O_2, thereby enhancing the stability of the catalyst [26], but also establishes strong electronic interactions with adjacent active sites. However, there have been few reports on the utilization of Cr to enhance the ORR activity and durability of Fe-based SACs.

Herein, we propose a one-step pyrolysis method to construct Cr ACs modified Fe SAs co-embedded on N, S co-doped carbon substrates (Cr_{AC}-Fe_1/N-S-C). The effective integration of Cr ACs and Fe SAs into the N, S co-doped carbon (N-S-C) material was demonstrated through aberration-corrected high-angle annular dark-field scanning transmission electron microscopy (HAADF-STEM) and X-ray absorption spectroscopy (XAS) analysis. More specifically, the Fe SAs modified with Cr ACs (referred to as Cr_{AC}-Fe_1/N-S-C) not only exhibited enhanced ORR activity, as indicated by a half-wave potential ($E_{1/2}$) of 0.88 V, but also displayed excellent durability over 100,000 voltage cycles. And the catalyst retained 81% of its initial current after a continuous 50-hour operation period. Delving into the mechanism, the incorporation of Cr ACs sites serves a dual role. First, it fine-tunes the electronic configuration around the Fe site, optimizing the intermediates' binding energy to the Fe site and accelerating the overall ORR kinetic process. Secondly, the Cr-Ac sites effectively suppress the Fenton reaction and rapidly eliminate generated ROS, and reduce Fe leaching at the neighboring Fe sites, thereby stabilizing the Fe site. After undergoing additional processing and being applied to zinc-air batteries, the sample demonstrates a substantial power density of 241 mW cm^{-2}, thereby facilitating uninterrupted operation for a duration surpassing 500 h. This discovery uncovers novel dimensions of the configurational connections between clusters consisting of varying metal centers and SAs, while also establishing a fresh pathway towards the synthesis of remarkably enduring ORR catalysts suitable for practical implementations.

2. Experimental section

2.1. Chemicals

Without further purification, the following materials were utilized: iron chloride hexahydrate ($FeCl_3 \cdot 6\ H_2O$, 99%, Aladdin), chromium trichloride ($CrCl_3 \cdot 6\ H_2O$, 98%, Aladdin), Melamine ($C_3H_6N_6$, Macklin), N-acetylcysteine ($C_5H10N2O2S$, Aladdin), PEG-PPG-PEG Pluronic P123 (Mw = 5800) (Sigma-Aldrich). The catalyst Pt (20% Pt supported on Vulcan XC-72 carbon) and Nafion (5.0 wt%) were acquired from Sigma-Aldrich. Deionized water was used in all experiments.

2.2. Synthesis of Cr_{AC}-Fe_1/N-S-C catalyst

A solution containing 5 g melamine, 0.156 g N-Acetyl-cysteine, 0.5 mg P123, 0.5 mg $FeCl_3 \cdot 6\ H_2O$ and 0.5 mg $CrCl_3 \cdot 6\ H_2O$ in 50 mL deionized solution was dissolved and subjected to continuous mixing for 6 h at a temperature of 80 °C. Drying of the precursor obtained was then carried out overnight in a desiccator at 100 °C, followed by carbonization under a stream of N_2 gas at a temperature of 950 °C for 2 h at a ramp rate of 10 °C min^{-1}. After carbonization, the resulting product was the Cr_{AC}-Fe_1/N-S-C material, obtained through the co-embedding of atomic level Cr ACs and Fe SAs on N-S-C material. The S-free Cr-Fe/N-S-C was prepared by a similar route to Cr_{AC}-Fe_1/N-S-C but without the introduction of a S source.

2.3. Synthesis of Fe_1/N-S-C catalyst

Fe_1/N-S-C is manufactured using the same process as Cr_{AC}-Fe_1/N-S-C, which involves incorporating single Fe atoms onto N-S-C substrates. Notably, the preparation process of Fe_1/N-S-C did not include the use of $CrCl_3 \cdot 6\ H_2O$.

2.4. Synthesis of Cr_{AC}/N-S-C catalyst

Cr_{AC}/N-S-C was synthesized using a procedure similar but different from Cr_{AC}-Fe_1/N-S-C, in which Cr clusters were deposited on N-S-C substrates. However, it is important to note that their synthesis method did not involve the use of $FeCl_3 \cdot 6\ H_2O$.

2.5. Characterizations

The Cu Kα radiation (λ = 0.15418 nm) was used to obtain X-ray diffraction patterns on a Rigaku X-ray diffractometer D-MAX 2200 VPC, employing a scan step size of 10 (°s^{-1}). Dark-field STEM, TEM, HRTEM images and EDS mapping were carried out using an FEI Tecnai G2 F30 microscope operating at 300 kV. X-ray photoelectron spectroscopy (XPS) measurements were conducted utilizing an ESCA Lab250 spectrometer that was outfitted with a two-anode Al Kα (1486.6 eV) X-ray source. The software Athena and Artemis were employed for the purposes of data reduction, data analysis, and EXAFS fitting. A standard film was used as a reference to calibrate the energy of the sample. The global amplitudes (CN, R, σ^2 and ΔE_0) for the extended X-ray absorption fine structure (EXAFS) were determined in reciprocal space through nonlinear least squares fitting of the EXAFS fitting equation to the Fourier transformed data, implementing the Artemis software. The EXAFS of the film was graphed, and the resulting amplitude reduction factor (S_0^2) was utilized in the EXAFS analysis to determine the coordination numbers (CNs) within the scattering path of the sample. The Debye-Waller factors and delta Rs are determined by utilizing the estimated parameters and constrained paths. Additionally, a wavelet transform (WT) is employed by utilizing the software package developed by Funke and Chukalina. The Morlet wavelet with κ = 10 and σ = 1 is applied in this process. Inductively Coupled Plasma Optical Emission Spectroscopy (ICP-OES) was carried out using an AGILENT 725-ES instrument to determine the Fe content and Cr contents of the samples. Inductively coupled plasma mass spectrometry (ICP-MS) was performed using an iCAP Q (Thermo Fisher Scientific) instrument, to determine the Fe content of the dissolution in the Cr_{AC}-Fe_1/N-S-C and Fe_1/N-S-C system for different test periods at 0, 3, 5, and 10 h. EPR measurements were conducted on a Bruker-A300 spectrometer. Before the electrochemical reaction, DMPO needs to be added in advance, and the concentration is controlled at about 100 mM. At the end of the cyclic voltammetric scan, 100 μL of the reaction solution was taken and 20 μL of pure DMPO was added, mixed, and then the tube was sealed by capillary loading for testing.

2.6. Electrode preparation and electrocatalytic measurement

AutoLab workstation is used to collect electrochemical data from a three-electrode measurement system. A carbon rod and an Ag/AgCl electrode were employed for the counter and reference electrodes, respectively. Subsequently, the electrode is made by weighing 5 mg of the powdered sample catalyst and dissolving it in a solution consisting of 20 μL of an aqueous 5 wt% Nafion solution, to 336 μL of isopropanol and to 144 μL of deionized water. To achieve a uniformly dispersed state, the catalyst slurry should then be ultrasonicated for 30 min. Afterwards, a volume of 16 μL of the ink was transferred onto the glassy carbon (GC) electrode, which possessed a surface area measuring 0.19625 cm^2, and subsequently subjected to drying through the application of infrared light. The experiments on ORR polarization were conducted utilizing either 0.1 M $HClO_4$ or 0.1 M KOH electrolyte with a sweep rate of 5 mV s^{-1}. For this investigation, all potentials have been recalibrated in

relation to reversible hydrogen potential (E_{RHE}). The Nernst equation was utilized to adjust all prospective measurements for the E_{RHE}, where E_{RHE} is equal to $E_{RHE} = E_{Ag/AgCl} + 0.198 + 0.059$ pH. The accelerated lifespan was assessed by alternating between voltage levels of 0.6 and 1.0 V, utilizing a scan rate of 100 mV s^{-1}, within an electrolyte saturated with oxygen, which comprised of either a 0.1 M KOH or a 0.1 M HClO$_4$ solution. The Koutecky-Levich Eqs. (1), (2), and (3) were utilized to ascertain the kinetic current (J_k):

$$\frac{1}{J} = \frac{1}{JL} + \frac{1}{JK} = \frac{1}{B\omega^{0.5}} + \frac{1}{JK} \tag{1}$$

$$B = 0.62nFC0(D0)^{2/3}\nu^{-1/6} \tag{2}$$

$$J_K = nFkC_0 \tag{3}$$

The presently observed density of electric current, designated as J, is established in correlation with the speed of electrode rotation, conveyed in the unit of radians per second. The value of B is determined through the calculation of the slope from the Koutechy-Levichi plot, which is derived from the Levich equation (Eq. 2). J_L and J_K represent the current densities at which diffusion and kinetics act as the limiting factors, respectively. The variable "n" denotes the quantity of transferred electrons. "F" represents the Faraday constant, which is equivalent to 96,485 coulombs per mole. C_0 signifies the concentration of O$_2$ in the electrolyte, which stands at 1.26×10^{-6} moles per cubic centimeter. D_0 represents the diffusion coefficient of O$_2$ in a solution of 0.1 M KOH or 0.1 M HClO$_4$. It possesses a numerical value of 1.93×10–5 square centimeters per second. Lastly, v symbolizes the kinetic viscosity, which holds a numerical value of 0.01009 square centimeters per second. The equations detailed here were employed to calculate the percentage of peroxide and the electron transfer number (n) for the RRDE measurements:

$$HO_2^- \% = 200 \times \frac{IR/N}{ID + IR/N} \tag{4}$$

$$n = 4 \times \frac{ID}{ID + IR/N} \tag{5}$$

The current collection effectiveness of the Pt ring, indicated as N, has been determined to be 0.40, where I_d refers to the current of the disk and I_r refers to the current of the ring.

2.7. Fenton-like reactivity measurements

The prepared Cr$_{AC}$-Fe$_1$/N-S-C or Fe$_1$/N-S-C catalysts were ultrasonically dispersed in 0.1 M HClO$_4$ to form a homogeneous suspension of 40 μg mL^{-1}. Appropriate amounts of 2,20-azinobis (3-ethylbenzthiazoline-6-sulfonate) (ABTS) and H$_2$O$_2$ were then added at concentrations of 2 and 20 millimolar (mM), respectively. After 7 min of reaction, the solution was centrifuged. The supernatant was diluted with 0.1 M HClO$_4$ (1:100) and characterized by UV–vis spectroscopy (HITACHI U-5100 UV–vis spectrophotometer). The level of ROS species produced during the H$_2$O$_2$ treatment of Cr$_{AC}$-Fe$_1$/N-S-C or Fe$_1$/N-S-C is evaluated by monitoring the change in absorbance at 415 nm.

2.8. Zinc-air battery performance test

The catalyst ink was prepared by utilizing ultrasonic dispersion to disperse 5 mg of catalyst powder and 20 μL of a Nafion solution, with a weight percentage of 5, in a blended solvent comprising isopropanol and water, with a volumetric ratio of 7 to 3. This procedure was conducted over a duration of 30 min. In the instance of a liquid zinc-air battery, the cathode that is made up of carbon paper was coated with an electrode possessing a loading of 2.5 mg cm^{-2}. The anode was composed of a zinc plate, and the electrolyte was made up of a solution of 6 M potassium hydroxide and 0.2 M zinc acetate in water. The experimentation on the

zinc-air batteries was conducted using an AutoLab workstation. In the context of assembling an all-solid-state zinc-air battery, the procedure for preparing the electrolyte-film in the all-solid-state zinc-air battery module involves the following steps: weighing ZnO (0.25 M), KOH (11.25 M), and N, N´-methylene-bisacrylamide (0.08 g), and subsequently dissolving them in 480 μL of acrylic acid. Then, this solution is added to the mixing solution while vigorously stirring. Then, a small amount of the mixture was extracted with a pipette gun, poured onto a fluted glass slide, and 30 μL of 0.3 M Ammonium persulfate was given to this and an electrolyte gel film was allowed to form for 10 min.

3. Results and discussions

3.1. Preparation and characterization

Rationalizing the Fe-N$_4$ active site electronic structure via incorporation of metal ACs is a promising strategy, due to the different electronic states of Fe SAs and ACs with different metal centers [32]. Hence, we constructed Fe-based SACs and Cr-based ACs by a combination of heteroatom doping and pyrolysis. Briefly, the Fe and Cr salts, N and S sources and surfactant P123 were dissolved in 50 mL of deionized water, stirred for 6 h, dried and then pyrolyzed at 950 °C. During this high temperature pyrolysis, small molecules in the precursors self-assembled to form Cr ACs and Fe SAs by co-anchoring the ligands with N and S heteroatoms. Fourier transform infrared (FTIR) spectroscopy in Fig. S1 shows that thiophene rings (C-S-C), C=C, C-N/C-O, -C=S- are present in all samples after pyrolysis at 950 °C. The strategy for the synthesis of Cr ACs-modified Fe SAs co-embedded on N-S-C material (Cr$_{AC}$-Fe$_1$/N-S-C) is shown in Fig. 1a. For comparison, S-free Cr-Fe/N-C, Cr$_{AC}$/N-S-C, Fe$_1$/N-S-C and N-S-C were also produced by a similar process. The X-ray diffraction (XRD) patterns acquired from the samples reveal the existence of two graphitic carbon peaks at angles of 26° and 44° [33], and all samples show no crystalline metallic Cr and/or Fe species peaks (Fig. 1b).

The dark-field STEM and TEM image of Cr$_{AC}$-Fe$_1$/N-S-C confirms the presence of a sheet-like graphitic carbon structure with a well-defined pore structure (Fig. 1c, and Fig. S2). Similar morphology is also observed in Fe$_1$/N-S-C and Cr$_{AC}$/N-S-C samples (Fig. S3). No metal particles or clusters were observed in all the prepared samples. Note that for the S-free Cr-Fe/N-S-C samples, as shown in Fig. S4, the catalyst clearly shows some aggregation. From previous reports, there is evidence that introduction of S atoms are conducive to hinder the diffusion of metal atoms and avoid the agglomeration [34] after annealing at 950 °C. The Raman spectroscopic analysis, as shown in Fig. S5, reveals no discernible discrepancies in the structural defects found within the graphitic plane among all catalysts. This is substantiated by the roughly equal proportion of peak intensities detected in the D-band (1350 cm^{-1}) and the G-band (1590 cm^{-1}), which respectively represent defective and graphitic carbon [35]. The porous characteristic of Cr$_{AC}$-Fe$_1$/N-S-C is additionally validated through Brunauer-Emmett-Teller (BET) analyses (refer to Fig. S6). The analyses indicate a considerably extensive specific surface area of 356.8 m^2 g^{-1}, accompanied by a range of pore diameters starting from 2.1 nm up to 62.8 nm (consult Table S1). The existence of such a porous configuration augments the accessibility to catalytically active sites and facilitates the transportation of reactants [36]. The elemental mapping of Cr$_{AC}$-Fe$_1$/N-S-C by energy dispersive X-ray spectroscopy (EDS) corresponding to the dark-field STEM image shows the coexistence of the elements C, N, O, S, Cr and Fe on Cr$_{AC}$-Fe$_1$/N-S-C ((Fig. 1c and Fig. S7). However, it is not possible to directly observe Cr clusters and Fe atoms because the contrast between small-sized clusters and atomic sites is like that of carbon in HRTEM (Fig. 1d and Fig. S8a-b). In order to corroborate the simultaneous existence of Cr ACs and atomically dispersed Fe SAs in the N-S-C support, HAADF-STEM images were performed. The HAADF-STEM images clearly demonstrate the presence of metal atomic sites and clusters (indicated by red and green circles) on the carbon surface, which are discernible as bright dots,
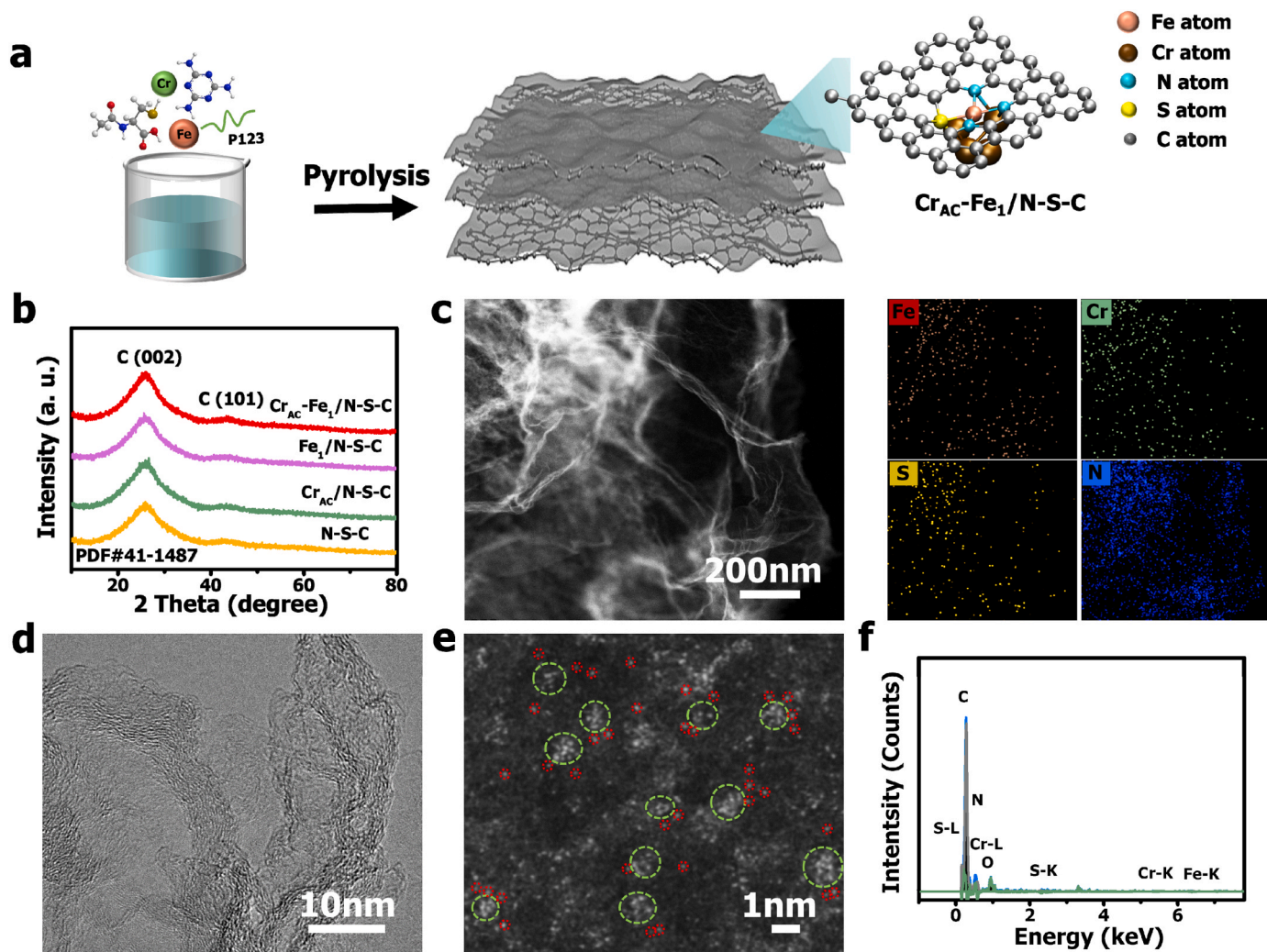
Fig. 1. Synthetic procedure and structural characterizations. (a) Schematic illustration for the preparation of Cr_{AC}-Fe_1/N-S-C. (b) XRD patterns of the N-S-C, Cr_{AC}/N-S-C, Fe_1/N-S-C, and Cr_{AC}-Fe_1/N-S-C. (c) Dark-field STEM image, and corresponding elemental mapping of the Cr_{AC}-Fe_1/N-S-C. (d) HRTEM image, (e) HAADF-STEM image, and (f) corresponding EDS spectrum of Cr_{AC}-Fe_1/N-S-C.

indicating the co-occurrence of Cr ACs and atomically dispersed Fe SAs within the carbon structure, as also observed in Fig. 1e and Fig. S8c-d. In particular, the size of the clusters is 1–2 nm, indicating that they are composed of multiple Cr atoms. Atomic resolution EDS images of Cr_{AC}-Fe_1/N-S-C further confirm that the Cr element is present in a state of ACs surrounded by discrete Fe atoms (Fig. 1f and Fig. S9). In addition, the presence of Cr and Fe was further confirmed by ICP-OES with 0.7 wt % Cr and 0.82 wt% Fe on the NC supports (See Table S2).

XPS characterization was employed to examine the surface chemical composition and structure of the catalysts in their initial state, as referenced in Table S3. The XPS spectrum of Cr_{AC}-Fe_1/N-S-C exhibited discernible signals for the elements C, N, O, S, Cr, and Fe, thereby corroborating the findings of the EDS elemental mapping, as illustrated in Fig. S10. The C 1 s XPS spectra of the three samples (Fig. S11) demonstrated the occurrence of three peaks with binding energies of 284.7, 285.7, and 288.6 eV electron volts, denoting the existence of C-C, C-N, and C-O bonds, respectively. As depicted in Fig. S12a, The N 1 s high-resolution spectra of the prepared Cr_{AC}-Fe_1/N-S-C exhibited decomposition into five distinct peaks, which corresponded to oxidized-N (402.6 eV), graphitized-N (400.9 eV), pyrrolic-N (399.2 eV), metal-N (398.3 eV), and pyridinic-N (397.8 eV) [37]. Meanwhile, the presence of Fe-N, Cr-N peaks was confirmed in Fe_1/N-S-C and Cr_{AC}/N-S-C samples (Fig. S12b-c). According to the findings in Fig. S13a, it is feasible to parse the high-resolution S 2p XPS spectrum into four distinct peaks with

energy levels recorded at 168.4, 164.8, 163.8, and 162.3 electron volts. These peaks can be categorized as C-SOx-C, S $2p_{1/2}$, S $2p_{3/2}$, and Fe/Cr-S, correspondingly [38]. Similar results were obtained in samples Fe_1/N-S-C and Cr_{AC}/N-S-C in Fig. S13b-c. The presence of Cr and Fe signals is affirmed in the Fe 2p (Fig. S14a) and Cr 2p (Fig. S14b) spectra. It is noteworthy that no zero-valent elemental Cr and Fe species were observed, implying that the Cr and Fe atoms are predominantly in alignment with the surrounding atoms.

A comprehensive analysis was performed using spectroscopic techniques, specifically XANES and EXAFS analysis. The purpose of this analysis was to thoroughly investigate the chemical state and coordination environment of Cr and Fe species found in Cr_{AC}-Fe_1/N-S-C. Fig. 2a illustrates the near-edge absorption at the Fe-K edge as detected by XANES spectra of the Cr_{AC}-Fe_1/N-S-C catalyst. The striking similarity to the near-edge absorption observed in iron phthalocyanine (FePc) suggests the presence of the Fe-N_x moiety [39]. The primary peak detected at a distance of 1.52 Å in reciprocal space within the Fourier Transform EXAFS (FT-EXAFS) spectrum of the Fe K edge in Cr_{AC}-Fe_1/N-S-C, as illustrated in Fig. 2b, is due to the presence of Fe-N and Fe-S bonds [40]. Significantly, when compared to the Fe foil, the absence of a peak at 2.2 Å (indicating the Fe-Fe bond length) strongly indicates the existence of Fe atoms dispersed in Cr_{AC}-Fe_1/N-S-C rather than the creation of particulates or clusters. We performed quantitative least-squares fitting of EXAFS spectra to further determine the Fe
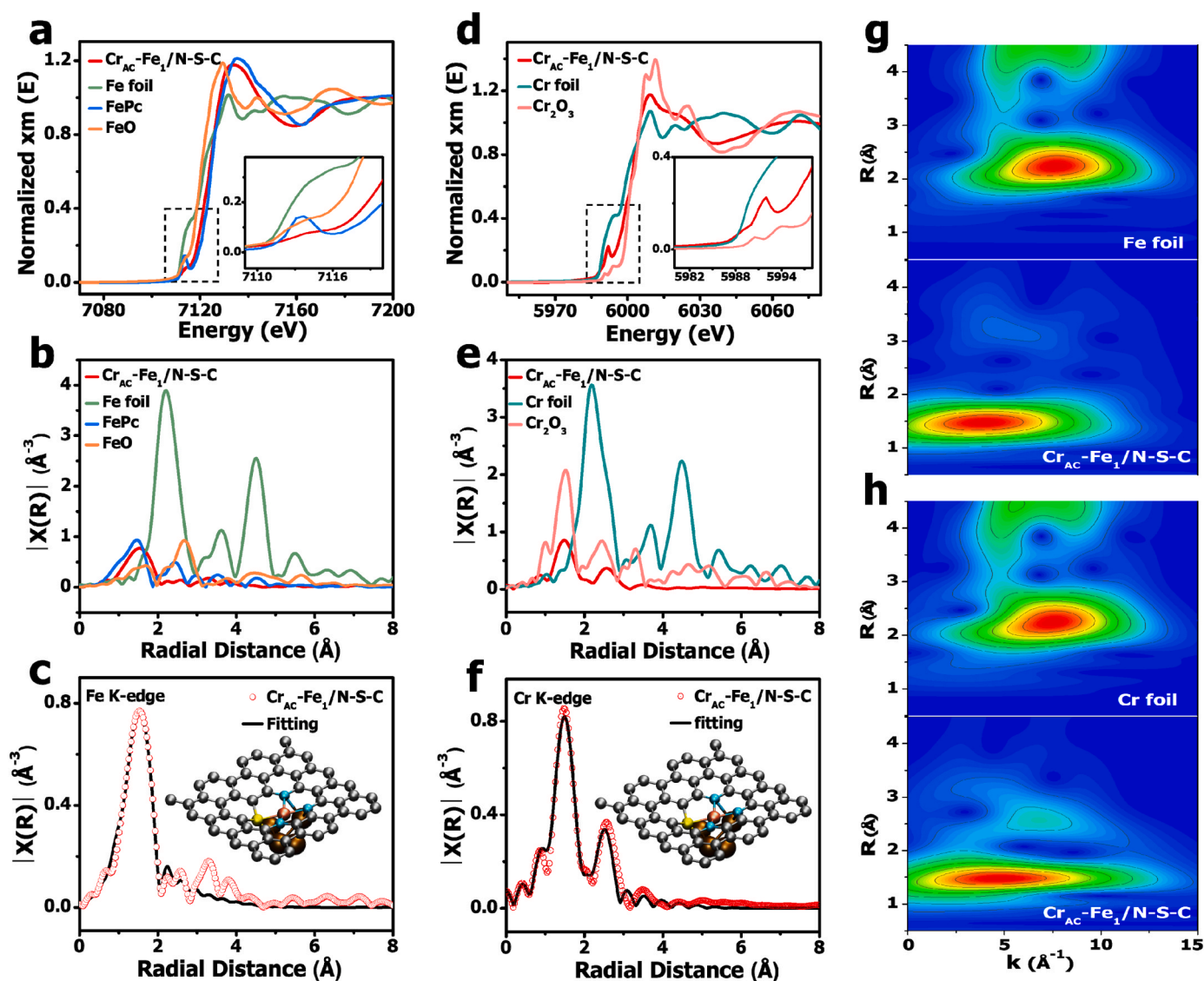
Fig. 2. Chemical state and atomic local structure of Cr_{AC}-Fe_1/N-S-C. (a) Normalized Fe K-edge XANES spectra and (b) Fe K-edge FT-EXAFS spectra of Cr_{AC}-Fe_1/N-S-C, Fe foil, FePc, and FeO. (c) Experimental and FT-EXAFS fitting curves of Cr_{AC}-Fe_1/N-S-C at Fe K-edge, inset is the corresponding schematic model (Fe: pink, N: blue, S: yellow and C: grey). (d) Normalized Cr K-edge XANES spectra and (e) Cr K-edge FT-EXAFS spectra of Cr_{AC}-Fe_1/N-S-C, Cr foil, and Cr_2O_3. f) Experimental and FT-EXAFS fitting curves of Cr_{AC}-Fe_1/N-S-C at Cr K-edge, inset is the corresponding schematic model (Cr: brown, N: blue, S: yellow and C: grey). (g-h) Wavelet transform of the k^3-weighted EXAFS data of Cr_{AC}-Fe_1/N-S-C, Fe foil, and Cr foil.

coordination configuration. Based on the depicted evidence in Fig. 2c and Fig. S15a, it has been confirmed through Fe K-edge EXAFS analysis and curve fitting of the R space imaginary component and k space that the Fe atoms are coordinated with three N atoms and one S atom in their first shell. Furthermore, the Fe-N and Fe-S coordination numbers were estimated to be 2.8 and 1.3, respectively, resulting in the formation of the Fe-N_3S_1 model (refer to Table S4 for details).

The figure presented in Fig. 2d illustrates the adsorption fine structure of the Cr-K edge. It shows that the Cr species within Cr_{AC}-Fe_1/N-S-C shift towards higher energies compared to Cr, as for the Cr_2O_3. This indicates that the Cr atoms have a positive charge and an oxidation state of approximately $+3$ [26]. The Cr K edge FT-EXAFS spectrum in Cr_{AC}-Fe_1/N-S-C exhibits a major peak at 1.49 Å (Fig. 2e), a shoulder peak at 2.06 Å, which are characteristic of the Cr-N and Cr-S coordination in the first shell. It is noteworthy that the intensity of the Cr-Cr bond peak in Cr_{AC}-Fe_1/N-S-C is noticeably lower compared to that in the Cr foil. This discrepancy can be attributed to the remarkably diminutive size of the Cr ACs (with a coordination number of 1.4, as shown in Table S5) and the absence of structural periodicity as

previously observed in other metal ACs. This corresponds to the HAADF-STEM results and further confirms the presence of ACs of Cr. The fitting results of the Cr K-edge in R- and k-space are shown in Fig. 2f, Fig. S15b and Table S5. Notably, the coordination numbers of Cr-N and Cr-S for Cr_{AC}-Fe_1/N-S-C were estimated to be 2.5 and 0.5, respectively. WT-EXAFS was utilized to explore the atomic dispersion of the Cr and Fe sites, employing the effective resolution in both the k- and R-spaces of the WT analysis. The WT-EXAFS contour plots (Fig. 2g and Fig. S15c) demonstrate that the Fe K-edge EXAFS spectrum exhibits the highest intensity at 3.8 Å^{-1} for Cr_{AC}-Fe_1/N-S-C in k-space. The presence of Fe-N and Fe-S bonds is responsible for this observation. The atomic configuration of Cr_{AC}-Fe_1/N-S-C was further investigated using the Cr-K edge WT-EXAFS technique. As shown in Fig. 2h and Fig. S15d, two intensity peaks at 4.6 Å^{-1} and 6.8 Å^{-1} correspond to the Cr-N/Cr-S and Cr-metal scattering paths, respectively, in the WT contour plots of Cr_{AC}--Fe_1/N-S-C. Notably, the waveform plots of WT are markedly different from those of the Cr foil, reflecting that the isolated Cr atoms are in clusters and not Cr-based crystalline structure in Cr_{AC}-Fe_1/N-S-C.

3.2. Electrocatalytic properties

Using an O_2-saturated 0.1 M KOH solution, the catalysts obtained were evaluated for ORR activity [41]. According to the data presented in Fig. 3a, the catalyst named Cr_{AC}-Fe_1/N-S-C demonstrated the highest ORR performance with an $E_{1/2}$ value of 0.88 V vs. RHE out of all the catalysts prepared. This performance surpassed that of the commercial Pt/C catalyst with an $E_{1/2}$ value of 0.85 V, as well as the N-C catalyst with an $E_{1/2}$ value of 0.60 V, the N-S-C catalyst with an $E_{1/2}$ value of 0.83 V, the Cr_{AC}/N-S-C catalyst with an $E_{1/2}$ value of 0.84 V, and the Fe_1/N-S-C catalyst with an $E_{1/2}$ value of 0.875 V. According to the Tafel curves depicted in Fig. S16, the Cr_{AC}-Fe_1/N-S-C exhibits the most minimal Tafel slope with a value of 74 mV dec^{-1}, indicating fast ORR kinetics or the lowest overpotential in the ORR process [42]. The double layer capacity of Cr_{AC}-Fe_1/N-S-C is proportional to the electrochemical surface area, surpassing that exhibited by Fe_1/N-S-C and Cr_{AC}/N-S-C (as illustrated in Fig. 3b and Fig. S17). These findings suggest that the existence of Cr ACs enhances the ORR performance of the Fe sites. The Koutecky-Levich (K-L) plots effectively showcased that the catalysts currently being examined exhibited the characteristics of first order reaction kinetics. By examining Fig. 3c, it was determined that the n of Cr_{AC}-Fe_1/N-S-C is approximately 4, thereby confirming the occurrence of the 4e⁻ ORR pathway. Additionally, the n and peroxide yields were assessed using the rotating ring disc electrode (RRDE) method (Fig. S18). The Cr_{AC}-Fe_1/N-S-C catalyst showcases an average n of 4.13

and a minimal H_2O_2 yield (less than 12.9%) within the potential range of 0.3 to 0.9 V. The results observed for the Fe_1/N-S-C catalyst, including an n value of 4.18 and an H_2O_2 yield of less than 14.2%, are like those obtained for the Cr_{AC}-Fe_1/N-S-C catalyst. These findings suggest that the ORR process of both Cr_{AC}-Fe_1/N-S-C and Fe_1/N-S-C catalysts is predominantly influenced by the 4e⁻ transfer pathway, as for Pt/C in the relevant potential range. Having an outstanding catalytic selectivity pertaining to cathodic reactions in the face of fuel poisoning is paramount to achieving optimum efficiency of an ORR electrocatalyst. Fig. S19 depicts that after adding methanol to the electrolyte for about 400 s, Cr_{AC}-Fe_1/N-S-C maintained a slight current drop during 1000 s of continuous operation and showed better methanol resistance compared to Fe_1/N-S-C, Cr_{AC}/N-S-C and Pt/C samples.

3.3. Theoretical calculation

To gain a more comprehensive comprehension of the augmenting effect of Cr ACs and S atoms on the ORR activity of Fe SACs, a series of systematic density functional theory (DFT) calculations were conducted [43,44]. Three models with configurations of N-doped Fe SA (Fe-N_4), N, S co-doped Fe SA (Fe-N_3S_1), and Cr_4 modified Fe SAs on N-S-C substrates (Cr_4-$Fe_1N_3S_1$) were constructed as shown in Fig. S20-22. The structures of the ORR intermediates on these three models can be observed in Fig. S20-22, whereas the corresponding free energy profiles of the ORR are illustrated in Fig. 3d-e. For U = 0 V, the energy path is downward for
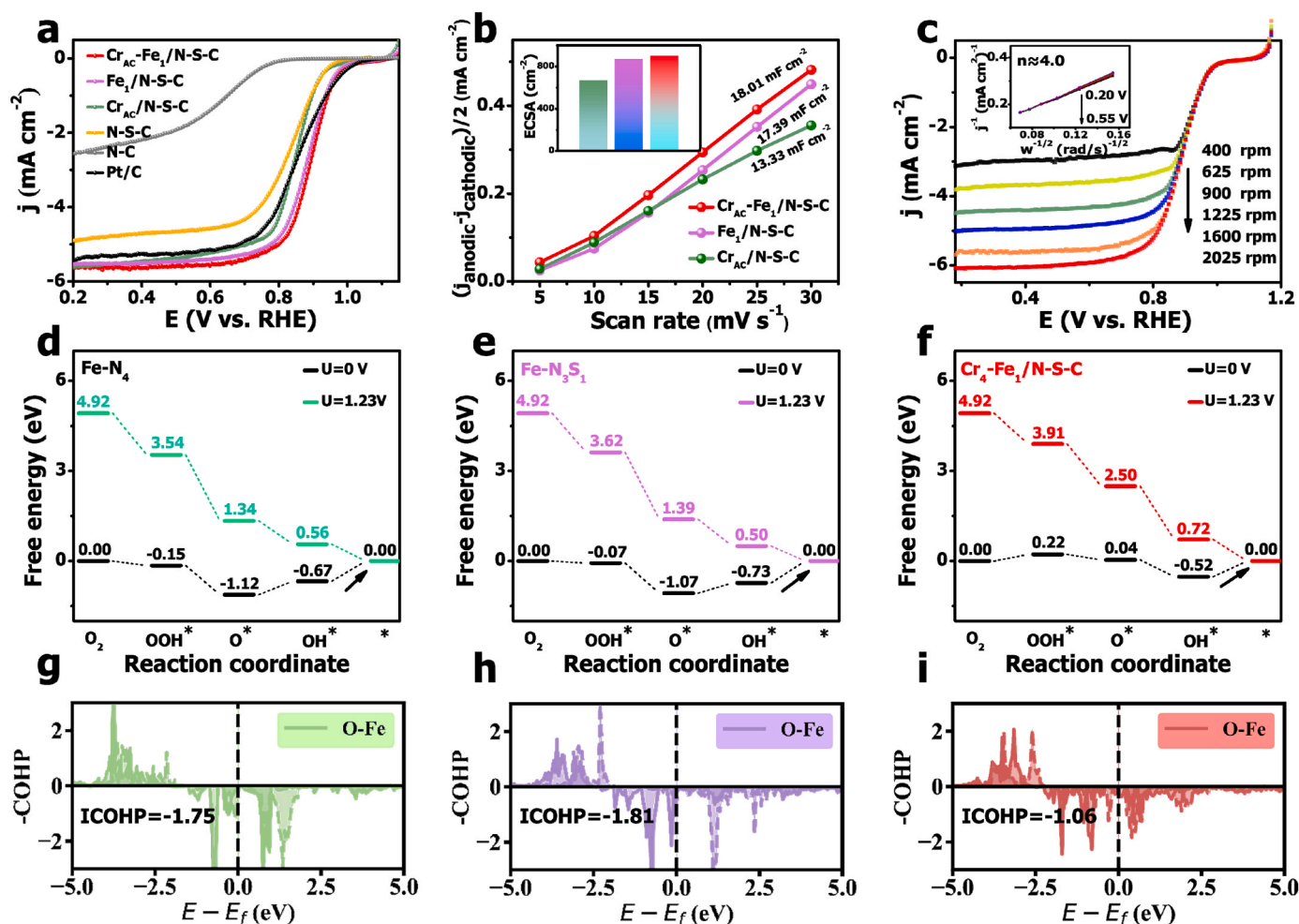

Fig. 3. Electrocatalytic performance and theoretical calculations. (a) LSV curves of the all catalysts in O_2-saturated 0.1 M KOH solution at a sweep rate of 5 mV s^{-1}. (b) Double-layer capacitances (C_{dl}) and inset of ECSA values. (c) LSV curves of Cr_{AC}-Fe_1/N-S-C at different rotating rates (inset: the corresponding K-L plots and electron transfer number). DFT calculations. (d-f) Gibbs free energy diagram for ORR on Fe-N_4, Fe-N_3S_1 and Cr_4-FeN_3S_1. COHP analysis and the corresponding ICOHP values of the O-Fe bond in (g) Fe-N_4, (h) Fe-N_3S_1 and (i) Cr_4-FeN_3S_1, respectively.

three samples, indicating a spontaneous and exothermic process. Upon raising the potential to 1.23 V, Cr_4-$Fe_1N_3S_1$ exhibits a lower overpotential of 0.52 V as opposed to Fe-N_4 (0.67 V) and Fe-N_3S_1 (0.73 V) (see Table S6), suggesting that the presence of Cr_4 and S atomic sites effectively adjusts the free energies of oxygen intermediate adsorption/desorption and diminishes the energy barrier for ORR. In three models, the rate-determining step (RDS) of ORR possessing the greatest uphill free energy takes place during the fourth electron transfer step (*OH + e$^-$ → OH$^-$), where *OH combines with an electron to form OH$^-$. Since the ORR performance follows the trend of Cr_4-$Fe_1N_3S_1$ > Fe-N_3S_1 based on the overpotential, we believe that the enhanced catalytic performance of Cr_4-$Fe_1N_3S_1$ can be attributed to the diminished interaction between *OH and the substrates participating in the RDS. Indeed, one can readily hypothesize that the collaboration between Cr_4 and S undermines the adhesive potency of Fe sites and *OH. The *d*-band center theory has been used extensively for the evaluation of the binding force between metal centers and adsorbates. Therefore, the spin up and spin down densities of states were calculated as shown in Fig. S23, among which the spin states with centers close to Fermi energy dominating the formation of chemical bond are selected for exploring the interaction strength between Fe and *OH [45]. As observed in Fig. S24 and Table S7, the *d*-band centers are considered as − 0.91 (spin down), − 0.81 (spin

down) and − 0.28 eV (spin up) for Cr_4-$Fe_1N_3S_1$, Fe-N_4 and Fe-N_3S_1, respectively. The decrease in the *d*-band center of the Fe sites causes a downward shift of the anti-bonding states and a corresponding augmentation in the level of occupancy, consequently leading to a lessening of the strength of the interaction between the metal centers and intermediates, and vice versa. The *d*-band center follows the trend of Cr_4-$Fe_1N_3S_1$ < Fe-N_4 < Fe-N_3S_1, implying that d-band center of Fe atom can serve as a good descriptor to predict the binding strength between Fe and *OH as well as the overpotential of ORR. To clarify the mechanism underlying the reduced binding strength of metal centers to *OH, the Fe-O intensity can be easily measured upon adsorption of OH. Crystal Orbital Hamiltonian (COHP) analysis was therefore carried out and integrated values of COHP (ICOHP) below the Fermi level were obtained to accurately assess the bonding strength between Fe-*OH. We show in Fig. 3g-i the COHP as well as the values of ICOHP of − 1.06, − 1.75 and − 1.81 for Cr_4-$Fe_1N_3S_1$, Fe-N_4 and Fe-N_3S_1, respectively. This demonstrates the interaction strength between Fe and *OH for three systems follow the trend of Cr_4-$Fe_1N_3S_1$ < Fe-N_4 < Fe-N_3S_1, which leads to the smallest uphill free energy of RDS for Cr_4-$Fe_1N_3S_1$. It should be noted that the COHP analysis was performed for those spin states with centers close to the Fermi level. Taken together, these findings underscore a significant improvement in the performance of Cr_{AC}-Fe_1/N-S-C in the
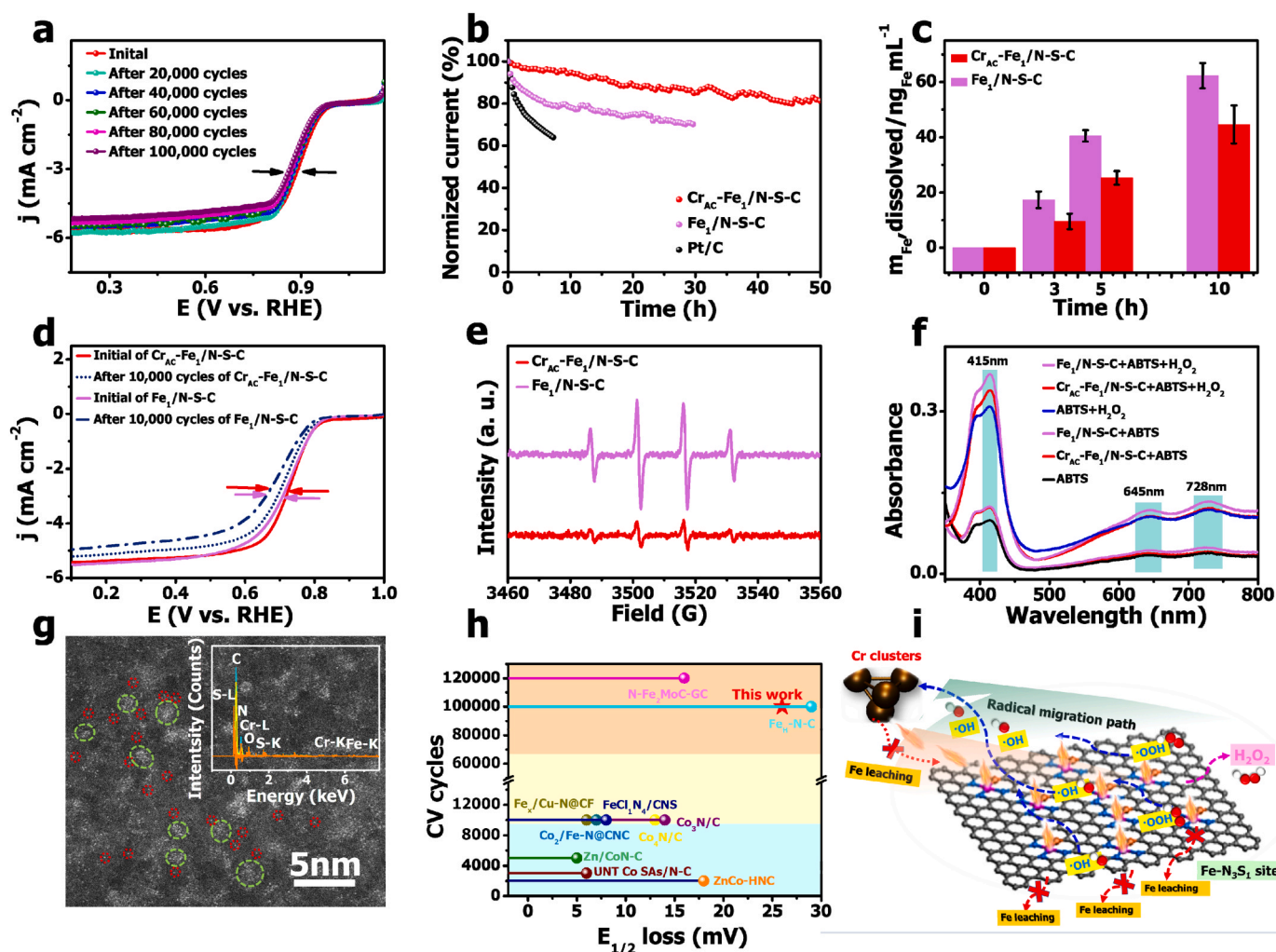
Fig. 4. Degradation mechanisms. (a) LSV curves of Cr_{AC}-Fe_1/N-S-C before and after 10,0000 potential cycles. (b) Normalized chronoamperometry curves of Cr_{AC}-Fe_1/N-S-C, Fe_1/N-S-C and Pt/C at constant potentials of 0.65 V. (c) Comparison of quantitative results of Fe dissolution in 0.1 M KOH for Cr_{AC}-Fe_1/N-S-C and Fe_1/N-S-C electrode after durability tests. (d) LSV curves of Cr_{AC}-Fe_1/N-S-C and Fe_1/N-S-C before and after CV cycles in 0.1 M HClO$_4$. (e) EPR spectra analysis of the ·OH elimination by Cr_{AC}-Fe_1/N-S-C and Fe_1/N-S-C. ·OH was generated by the ORR testing process and detected by DMPO. (f) Absorption spectrum of the ABTS radical cation with different catalysts. (g) HAADF-STEM image and corresponding EDS spectrum of Cr_{AC}-Fe_1/N-S-C after durability tests. (h) $E_{1/2}$ loss compared with recently reported excellent catalysts. (i) Schematic of Cr AC to protect Fe sites from ROS and slow Fe leaching.

ORR, owing to the inclusion of Cr ACs.

3.4. Degradation mechanisms

Durability is also an important consideration in the assessment of catalyst performance. Specifically, the Cr_{AC}-Fe_1/N-S-C catalyst showed excellent stability even after 100,000 cycles, as evidenced by an $E_{1/2}$ loss of only 26 mV (Fig. 4a). The increased stability is additionally supported by the chronoamperometry measurement (Fig. 4b). In this measurement, Cr_{AC}-Fe_1/N-S-C shows an impressive 81% preservation after 50 h of uninterrupted functioning. Besides, under the same alkaline conditions, the current retention of Fe_1/N-S-C was 70% after 30 h of operation, compared to 66.1% after 7.5 h of operation with commercial Pt/C. The results prove the excellent electrochemical catalytic stability of Cr_{AC}-Fe_1/N-S-C. To further investigate the Fe-N-C decomposition mechanism in alkaline ORR, the leaching of Fe is considered [46]. The Fe dissolution in Cr_{AC}-Fe_1/N-S-C and Fe_1/-S-C systems for different test periods at 0, 3, 5, 10 h is compared in Fig. 4c and Table S8. The results confirm that the presence of Cr ACs slows down the dissolution of Fe. Subsequently, the stability of the Cr_{AC}-Fe_1/N-S-C and Fe_1/-S-C catalysts was also evaluated in oxygen saturated 0.1 M $HClO_4$. Of note, the $E_{1/2}$ value of the Cr_{AC}-Fe_1/N-S-C catalyst exhibited a decrease of merely 22 mV after undergoing 10,000 cycles, which is significantly lower compared to the corresponding Fe_1/N-S-C catalyst (40 mV; illustrated in Fig. 4d). In order to evaluate the radical scavenging activity of the as-prepared Cr_{AC}-Fe_1/N-S-C and Fe_1/N-S-C catalysts, we employed EPR analyses were conducted with a nitrone spin trap (5,5-dimethyl-1-pyrroline N-oxide, DMPO) during ORR CV cycling [47]. Fig. 4e shows that the intensity of the Cr_{AC}-Fe_1/N-S-C EPR peak with Cr ACs decreased significantly compared to Fe_1/N-S-C without Cr ACs. Furthermore, we next compared the Fenton reactivity of Fe-N-C and Cr_{AC}-Fe_1/N-S-C catalysts using ABTS as a probe (Fig. 4f) [28,31]. Interestingly, the absorbance value of Cr_{AC}-Fe_1/N-S-C was lower than that of Fe_1/N-S-C at 415 nm, 645 nm, and 728 nm. We therefore deduce that the superb stability of Cr_{AC}-Fe_1/N-S-C originates from its low activity to catalyze the Fenton reaction, thus suffering less from oxidative damage by ROS. TEM and HAADF-STEM measurements were therefore carried out to examine and compare the morphological evolution of Cr_{AC}-Fe_1/N-S-C after the stability tests. From Fig. 4g and Fig. S25, one can see that the Cr ACs and Fe SAs sites are still well distributed on the carbon carrier without observable aggregation, pointing to the structural robustness and stability of Cr_{AC}-Fe_1/N-S-C. Excellent stability performance exceeds that previously reported for most transition metal catalysts under similar conditions (Fig. 4h and Table S9).

A ROS, such as the hydroxyl radical, is identified as a major deactivator of Fe-N-C catalysts operating from acidic to neutral pH environments [47]. This finding suggests that in order to ensure sustainable operation of fuel cells with Fe-N-C cathodes, it is essential to control the formation and lifetime of ROS at such pH levels. For Fig. 4i, the introduced Cr AC eliminates the formation of ·OH radicals at the Fe sites, thus reducing the survival time of the radicals and the area of the region where the radicals are destroyed. The introduction of Cr ACs effectively mitigated the degradation of Fe sites by free radicals and further enhanced the stability of Fe-based catalysts. Alternatively, we propose that the Fe dissolution from FeN_xC_y sites in alkaline media can be attributed to the instability of the coordinated Fe [46]. For Fe_1/N-S-C in alkaline media, the Fe redox transition induced by ORR destabilizes the atomic interface and potentially detaches the carbon shell from Fe, at least locally, causing this exposed Fe to dissolve. The presence of Cr ACs in the carbon substrate solves the problem of unstable Fe coordination structure. Cr_{AC}-Fe_1/N-S-C catalyst is conferred with outstanding stability due to a radical scavenging effect and slow down Fe leaching via Cr ACs introduction.
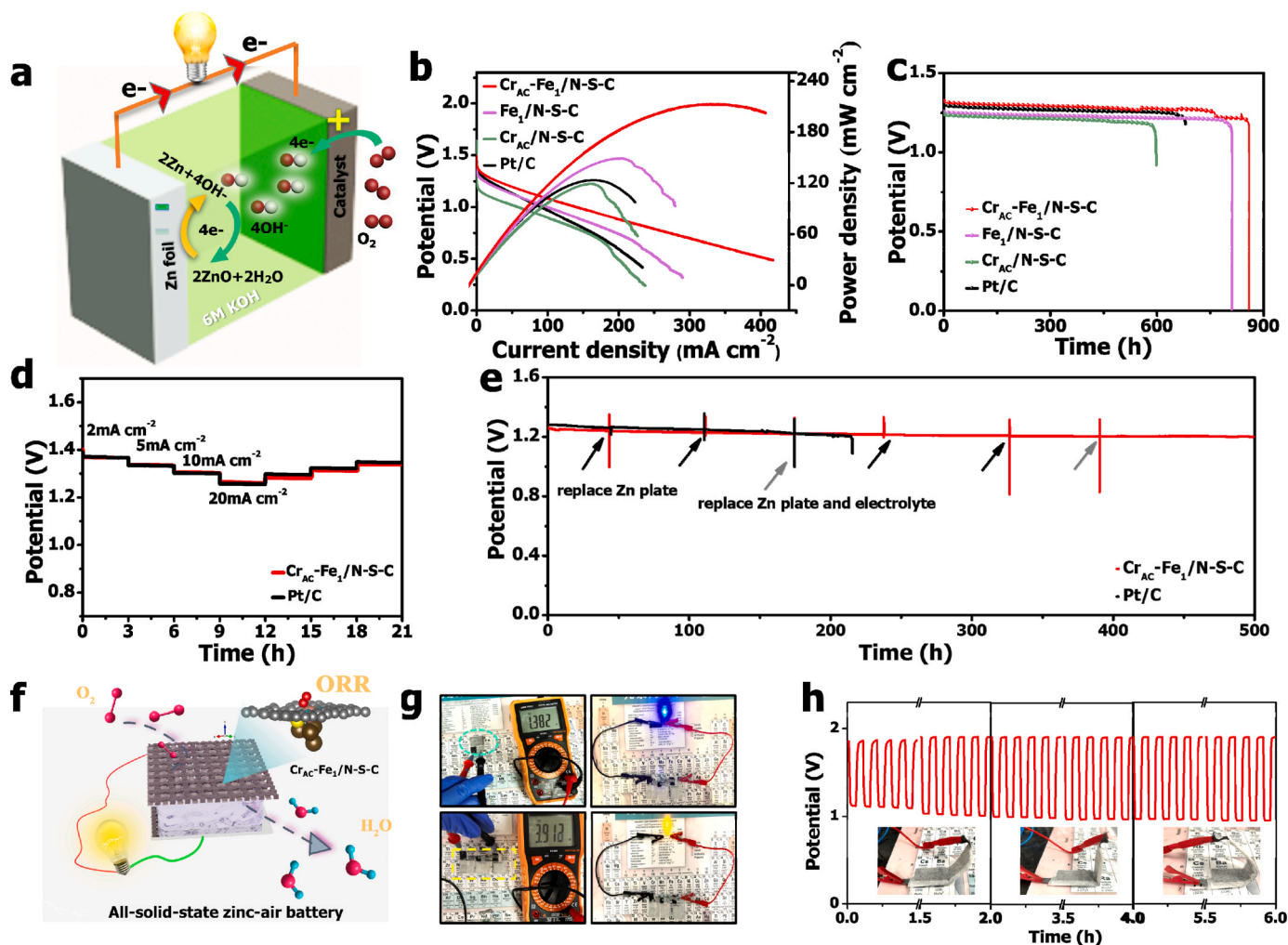
3.5. Zinc-air battery tests

Considering the excellent catalytic functionality of the all-prepared catalyst, we used the synthesized catalyst as a working air cathode, with zinc plate as the anodal component of the catalyst and 6 M KOH with 0.2 M $Zn(CH_3COO)_2$ as the electrolytic solution for pragmatic implementation (Fig. 5a) [48–51]. According to the information provided in Fig. 5b, the Cr_{AC}-Fe_1/N-S-C based zinc-air battery demonstrates a peak power density of 214.2 mW cm^{-2}, surpassing that of the benchmark Pt/C (124.7 mW cm^{-2}), Fe_1/N-S-C (150.1 mW cm^{-2}), and Cr_{AC}/N-S-C (120.6 mW cm^{-2}) based zinc-air batteries. Furthermore, when taking into account the zinc mass, the specific capacity of the Cr_{AC}-Fe_1/N-S-C battery is determined to be 858.2 mA h g$_{Zn}^{-1}$. This value surpasses that of the Pt/C (677.9 mA h g$_{Zn}^{-1}$), Fe_1/N-S-C (809.9 mA h g$_{Zn}^{-1}$), and Cr_{AC}/N-S-C (598.5 mA h g$_{Zn}^{-1}$) batteries, as illustrated in Fig. 5c. Fig. 5d illustrates that the discharge current density, ranging from 2 to 20 mA cm^{-2}, undergoes periodic changes every 3 h, indicating commendable rate capability. The battery's capacity is effectively renewed by reversing the current density from 10 to 2 mA cm^{-2}. In order to further investigate the electrochemical stability of the Cr_{AC}-Fe_1/N-S-C in the zinc-air battery, a galvanostatic discharge test was carried out at 5 mA cm^{-2} (Fig. 5e). From Fig. 5e, it is apparent that the discharge voltage of the Cr_{AC}-Fe_1/N-S-C battery demonstrates a negligible reduction throughout a period of 500 h, in contrast to the battery based on Pt/C. Notably, when the zinc plate and electrolyte are replenished, the voltage can return to its original state, further confirming the ultra-stable nature of Cr_{AC}-Fe_1/N-S-C. Subsequently, all-solid-state batteries are also assembled to extend the practical application of Cr_{AC}-Fe_1/N-S-C catalyst (Fig. 5f) [39]. According to the data presented in Fig. 5g, we conducted an experiment utilizing a solid-state battery with an open circuit potential of 1.38 V. By connecting three solid-state ZABs in a series configuration, it was observed that the potential can reach a maximum of 3.9 V, which is sufficient to illuminate blue and yellow LED bulbs. When subjected to a current density of 1 mA cm^{-2}, the solid-state batteries exhibit consistent voltage levels during the charging and discharging process for a duration of 2 h (as depicted in Fig. 5h). This remained true even when the batteries were bent at angles of 30°, 90°, and 120°. The above test results provide further confirmation regarding the exceptional practical implementation of Cr_{AC}-Fe_1/N-S-C in both liquid and fully solid-state flexible zinc-air batteries.

4. Conclusion

To sum up, we constructed atomically dispersed catalysts consisting of Cr ACs and Fe SAs polymetallic centers by using the heteroatoms N and S to optimize the coordination strength between the metal and the substrate during the pyrolysis treatment. Combined analyses of experimental and theoretical calculations verify that the introduction of the Cr ACs configuration is mainly responsible for the improvement of the high ORR performance of Fe SA sites. More importantly, this catalyst exhibits significant durability compared to the Fe counterpart due to the ability of the Cr ACs sites to scavenge free radicals and avoid the detrimental effects of the Fenton reaction, and slow down the Fe leaching from the coordination Fe sites on the carbon framework. Subsequently, the Zn-air battery with the Cr_{AC}-Fe_1/N-S-C catalyst demonstrated superior power density and remarkable cycling stability, suggesting its potential suitability for practical applications. This new catalyst is a promising avenue for the development of highly active and durable Fe-based ORR catalysts for SAC.

CRediT authorship contribution statement

Xiao Yuhang: Investigation, Methodology, Validation. **Tan Xiaohong:** Formal analysis, Validation. **He Weidong:** Data curation, Investigation, Validation. **Chen Jianpo:** Data curation, Formal analysis,

Fig. 5. Performance of zinc-air batteries for applications. (a) Schematic diagram of the configuration of a zinc-air battery. (b) LSV curves and power density plots. (c) Specific capacity. (d) Galvanostatic discharge of Cr_{AC}-Fe_1/N-S-C and Pt/C catalysts under various current density. (e) Long-term durability measurement of zinc-air battery assembled with Cr_{AC}-Fe_1/N-S-C cathode at 5 mA cm^{-2}. (f) Schematic structure of a solid-state flexible zinc-air batteries. (g) Photograph of battery the open circuit voltage, and the LED of three series-connected flexible zinc-air batteries. (h) Cycle performance under different bending conditions at 1 mA cm^{-2}.

Investigation, Methodology. **Li Yan:** Investigation, Methodology, Resources, Validation. **Cui Hao:** Conceptualization, Data curation, Funding acquisition, Resources, Validation, Visualization, Writing – review & editing. **Wang Chengxin:** Conceptualization, Funding acquisition, Resources, Writing – review & editing. **Guo Yingying:** Conceptualization, Data curation, Formal analysis, Investigation, Supervision, Validation, Visualization, Writing – original draft, Writing – review & editing. **Wang Chenhui:** Formal analysis, Funding acquisition, Resources, Supervision, Writing – review & editing.

Declaration of Competing Interest

We declare that we do not have any commercial or associative interest that represents a conflict of interest in connection with the work submitted.

Data availability

The data that support the findings of this study are available from the corresponding author upon reasonable request.

Acknowledgements

This work was financially supported by the National Natural Science

Appendix A. Supporting information

Supplementary data associated with this article can be found in the online version at doi:10.1016/j.apcatb.2023.123679.

References

[1] X. Tian, X.F. Lu, B.Y. Xia, X.W. Lou, Advanced electrocatalysts for the oxygen reduction reaction in energy conversion technologies, Joule 4 (2020) 45–68.

[2] W. Sun, F. Wang, B. Zhang, M. Zhang, V. Küpers, X. Ji, C. Theile, P. Bieker, K. Xu, C. Wang, M. Winter, A rechargeable zinc-air battery based on zinc peroxide chemistry, Science 371 (2021) 46–51.

[3] H. Adabi, A. Shakouri, N. Ul Hassan, J.R. Varcoe, B. Zulevi, A. Serov, J. R. Regalbuto, W.E. Mustain, High-performing commercial Fe–N–C cathode electrocatalyst for anion-exchange membrane fuel cells, Nat. Energy 6 (2021) 834–843.

[4] M. Shao, Q. Chang, J.-P. Dodelet, R. Chenitz, Recent advances in electrocatalysts for oxygen reduction reaction, Chem. Rev. 116 (2016) 3594–3657.

[5] R. Ma, G. Lin, Y. Zhou, Q. Liu, T. Zhang, G. Shan, M. Yang, J. Wang, A review of oxygen reduction mechanisms for metal-free carbon-based electrocatalysts, npj Comput. Mater. 5 (2019) 78.

[6] I. Gamba, Z. Codolà, J. Lloret-Fillol, M. Costas, Making and breaking of the OO bond at iron complexes, Coord. Chem. Rev. 334 (2017) 2–24.

[7] J. Wang, Z. Huang, W. Liu, C. Chang, H. Tang, Z. Li, W. Chen, C. Jia, T. Yao, S. Wei, Y. Wu, Y. Li, Design of N-coordinated dual-metal sites: a stable and active Pt-free catalyst for acidic oxygen reduction reaction, J. Am. Chem. Soc. 139 (2017) 17281–17284.

[8] S. Kattel, G. Wang, Reaction pathway for oxygen reduction on FeN4 embedded graphene, J. Phys. Chem. Lett. 5 (2014) 452–456.

[9] C. Wan, X. Duan, Y. Huang, Molecular design of single-atom catalysts for oxygen reduction reaction, Adv. Energy Mater. 10 (2020) 1903815.

[10] H. Yang, Y. Liu, X. Liu, X. Wang, H. Tian, G.I.N. Waterhouse, P.E. Kruger, S. G. Telfer, S. Ma, Large-scale synthesis of N-doped carbon capsules supporting atomicallydispersed iron for efficient oxygen reduction reaction electrocatalysis, eScience 2 (2022) 227–234.

[11] Y. Chen, S. Ji, C. Chen, Q. Peng, D. Wang, Y. Li, Single-atom catalysts: synthetic strategies and electrochemical applications, Joule 2 (2018) 1242–1264.

[12] Z. Chen, H. Niu, J. Ding, H. Liu, P.-H. Chen, Y.-H. Lu, Y.-R. Lu, W. Zuo, L. Han, Y. Guo, S.-F. Hung, Y. Zhai, Unraveling the origin of sulfur-doped Fe-N-C single-atom catalyst for enhanced oxygen reduction activity: effect of iron spin-state tuning, Angew. Chem., Int. Ed. 60 (2021) 25404–25410.

[13] K. Yuan, D. Lützenkirchen-Hecht, L. Li, L. Shuai, Y. Li, R. Cao, M. Qiu, X. Zhuang, M.K.H. Leung, Y. Chen, U. Scherf, Boosting oxygen reduction of single iron active sites via geometric and electronic engineering: nitrogen and phosphorus dual coordination, J. Am. Chem. Soc. 142 (2020) 2404–2412.

[14] Y. Guo, C. Wang, Y. Xiao, X. Tan, J. Chen, W. He, Y. Li, H. Cui, C. Wang, Increasing the number of modulated Fe single-atom sites by adjacent nanoparticles for efficient oxygen reduction with spin-state transition, Nano Energy 117 (2023) 108895.

[15] Y. Pan, X. Ma, M. Wang, X. Yang, S. Liu, H.-C. Chen, Z. Zhuang, Y. Zhang, W.-C. Cheong, C. Zhang, X. Cao, R. Shen, Q. Xu, W. Zhu, Y. Liu, X. Wang, X. Zhang, W. Yan, J. Li, H.M. Chen, C. Chen, Y. Li, Construction of N, P co-doped carbon frames anchored with fe single atoms and Fe2P nanoparticles as a robust coupling catalyst for electrocatalytic oxygen reduction, Adv. Mater. 34 (2022) 2203621.

[16] Z. Wang, X. Jin, C. Zhu, Y. Liu, H. Tan, R. Ku, Y. Zhang, L. Zhou, Z. Liu, S.-J. Hwang, H.J. Fan, Atomically dispersed Co2–N6 and Fe–N4 costructures boost oxygen reduction reaction in both alkaline and acidic media, Adv. Mater. 33 (2021) 2104718.

[17] X. Wei, S. Song, W. Cai, X. Luo, L. Jiao, Q. Fang, X. Wang, N. Wu, Z. Luo, H. Wang, Z. Zhu, J. Li, L. Zheng, W. Gu, W. Song, S. Guo, C. Zhu, Tuning the spin state of Fe single atoms by Pd nanoclusters enables robust oxygen reduction with dissociative pathway, Chem 9 (2023) 181–197.

[18] H. Tian, A. Song, P. Zhang, K. Sun, J. Wang, B. Sun, Q. Fan, G. Shao, C. Chen, H. Liu, Y. Li, G. Wang, High durability of Fe–N–C single-atom catalysts with carbon vacancies toward the oxygen reduction reaction in alkaline media, Adv. Mater. 35 (2023) 2210714.

[19] R. Jiang, L. Li, T. Sheng, G. Hu, Y. Chen, L. Wang, Edge-site engineering of atomically dispersed Fe–N4 by selective C–N bond cleavage for enhanced oxygen reduction reaction activities, J. Am. Chem. Soc. 140 (2018) 11594–11598.

[20] T. Asset, P. Atanassov, Iron-nitrogen-carbon catalysts for proton exchange membrane fuel cells, Joule 4 (2020) 33–44.

[21] Q. Ma, H. Jin, J. Zhu, Z. Li, H. Xu, B. Liu, Z. Zhang, J. Ma, S. Mu, Stabilizing Fe–N–C catalysts as model for oxygen reduction reaction, Adv. Sci. 8 (2021) 2102209.

[22] H. Sun, C.-W. Tung, Y. Qiu, W. Zhang, Q. Wang, Z. Li, J. Tang, H.-C. Chen, C. Wang, H.M. Chen, Atomic metal–support interaction enables reconstruction-free dual-site electrocatalyst, J. Am. Chem. Soc. 144 (2022) 1174–1186.

[23] D. Xia, X. Yang, L. Xie, Y. Wei, W. Jiang, M. Dou, X. Li, J. Li, L. Gan, F. Kang, Direct growth of carbon nanotubes doped with single atomic Fe–N4 Active sites and neighboring graphitic nitrogen for efficient and stable oxygen reduction electrocatalysis, Adv. Funct. Mater. 29 (2019) 1906174.

[24] H. Su, M.A. Soldatov, V. Roldugin, Q. Liu, Platinum single-atom catalyst with self-adjustable valence state forlarge-current-density acidic water oxidation, eScience 2 (2022) 102–109.

[25] H. Sun, L. Li, H.-C. Chen, D. Duan, M. Humayun, Y. Qiu, X. Zhang, X. Ao, Y. Wu, Y. Pang, K. Huo, C. Wang, Highly efficient overall urea electrolysis via single-atomically active centers on layered double hydroxide, Sci. Bull. 67 (2022) 1763–1775.

[26] E. Luo, H. Zhang, X. Wang, L. Gao, L. Gong, T. Zhao, Z. Jin, J. Ge, Z. Jiang, C. Liu, W. Xing, Single-atom Cr–N4 sites designed for durable oxygen reduction catalysis in acid media, Angew. Chem. Int. Ed. 58 (2019) 12469–12475.

[27] K. Kodama, T. Nagai, A. Kuwaki, R. Jinnouchi, Y. Morimoto, Challenges in applying highly active Pt-based nanostructured catalysts for oxygen reduction reactions to fuel cell vehicles, Nat. Nanotechnol. 16 (2021) 140–147.

[28] Y. Chu, E. Luo, Y. Wei, S. Zhu, X. Wang, L. Yang, N. Gao, Y. Wang, Z. Jiang, C. Liu, J. Ge, W. Xing, Dual single-atom catalyst design to build robust oxygen reduction electrode via free radical scavenging, Chem. Catal. 3 (2023) 100532.

[29] X. Zeng, J. Shui, X. Liu, Q. Liu, Y. Li, J. Shang, L. Zheng, R. Yu, Single-atom to single-atom grafting of Pt1 onto Fe–N4 center: Pt1@Fe–N–C multifunctional

[30] A. Han, W. Sun, X. Wan, D. Cai, X. Wang, F. Li, J. Shui, D. Wang, Construction of Co4 atomic clusters to enable Fe–N4 motifs with highly active and durable oxygen reduction performance, Angew. Chem. Int. Ed. 62 (2023) 5, e20230318.

[31] X. Cheng, X. Jiang, S. Yin, L. Ji, Y. Yan, G. Li, R. Huang, C. Wang, H. Liao, Y. Jiang, S. Sun, Instantaneous free radical scavenging by CeO2 nanoparticles adjacent to the Fe−N4 active sites for durable fuel cells, Angew. Chem. Int. Ed. 62 (2023) e202306166.

[32] C. Qi, H. Yang, Z. Sun, H. Wang, N. Xu, G. Zhu, L. Wang, W. Jiang, X. Yu, X. Li, Q. Xiao, P. Qiu, W. Luo, Modulating electronic structures of iron clusters through orbital rehybridization by adjacent single copper sites for efficient oxygen reduction, Angew. Chem. Int. Ed. (2023) e202308344.

[33] Y. Guo, P. Yuan, J. Zhang, Y. Hu, I.S. Amiinu, X. Wang, J. Zhou, H. Xia, Z. Song, Q. Xu, S. Mu, Carbon nanosheets containing discrete Co-Nx-By-C active sites for efficient oxygen electrocatalysis and rechargeable Zn-air batteries, ACS Nano 12 (2018) 1894–1901.

[34] P. Yin, X. Luo, Y. Ma, S.-Q. Chu, S. Chen, X. Zheng, J. Lu, X.-J. Wu, H.-W. Liang, Sulfur stabilizing metal nanoclusters on carbon at high temperatures, Nat. Commun., 12 (2021) 3135.

[35] W. Su, N. Kumar, A. Krayev, M. Chaigneau, In situ topographical chemical and electrical imaging of carboxyl graphene oxide at the nanoscale, Nat. Commun. 9 (2018) 2891.

[36] Y. Guo, P. Yuan, J. Zhang, H. Xia, F. Cheng, M. Zhou, J. Li, Y. Qiao, S. Mu, Q. Xu, Co2P–CoN double active centers confined in N-doped carbon nanotube: heterostructural engineering for trifunctional catalysis toward HER, ORR, OER, and Zn–air batteries driven water splitting, Adv. Funct. Mater. 28 (2018) 1805641.

[37] Y. Qiao, P. Yuan, Y. Hu, J. Zhang, S. Mu, J. Zhou, H. Li, H. Xia, J. He, Q. Xu, Sulfuration of an Fe–N–C catalyst containing FexC/Fe species to enhance the catalysis of oxygen reduction in acidic media and for use in flexible Zn–air batteries, Adv. Mater. 30 (2018) 1804504.

[38] Y. Li, S. Zhu, Y. Xu, R. Ge, J. Qu, M. Zhu, Y. Liu, J.M. Cairney, R. Zheng, S. Li, J. Zhang, W. Li, FeS2 bridging function to enhance charge transfer between MoS2 and g–C3N4 for efficient hydrogen evolution reaction, Chem. Eng. J. 421 (2021) 127804.

[39] W. Zhai, S. Huang, C. Lu, X. Tang, L. Li, B. Huang, T. Hu, K. Yuan, X. Zhuang, Y. Chen, Simultaneously integrate iron single atom and nanocluster triggered tandem effect for boosting oxygen electroreduction, Small 18 (2022) 2107225.

[40] L. Yu, Y. Li, Y. Ruan, Dynamic control of sacrificial bond transformation in the Fe−N−C single-atom catalyst for molecular oxygen reduction, Angew. Chem. Int. Ed. 60 (2021) 25296–25301.

[41] Q. Jin, B. Ren, J. Chen, H. Cui, C. Wang, A facile method to conduct 3D self-supporting Co-FeCo/N-doped graphene-like carbon bifunctional electrocatalysts for flexible solid-state zinc battery, Appl. Catal. B 256 (2019) 117887.

[42] M. Xiao, L. Gao, Y. Wang, X. Wang, J. Zhu, Z. Jin, C. Liu, H. Chen, G. Li, J. Ge, Q. He, Z. Wu, Z. Chen, W. Xing, Engineering energy level of metal center: Ru single-atom site for efficient and durable oxygen reduction catalysis, J. Am. Chem. Soc. 141 (2019) 19800–19806.

[43] D.G.A. Smith, L.A. Burns, K. Patkowski, C.D. Sherrill, Revised damping parameters for the D3 dispersion correction to density functional theory, J. Phys. Chem. Lett. 7 (2016) 2197–2203.

[44] H.J. Monkhorst, J.D. Pack, Special points for Brillouin-zone integrations, Phys. Rev. B 13 (1976) 5188–5192.

[45] M. Tachibana, K. Yoshizawa, A. Ogawa, H. Fujimoto, R. Hoffmann, Sulfur−gold orbital interactions which determine the structure of alkanethiolate/Au(111) self-assembled monolayer systems, J. Phys. Chem. B 106 (2002) 12727–12736.

[46] Y. Ku, K. Ehelebe, A. Hutzler, M. Bierling, T. Böhm, A. Zitolo, M. Vorokhta, N. Bibent, F.D. Speck, D. Seeberger, I. Khalakhan, K. Mayrhofer, S. Thiele, F. Jaouen, S. Cherevko, Oxygen reduction reaction in alkaline media causes iron leaching from Fe-N-C electrocatalysts, J. Am. Chem. Soc. 144 (2022) 9753–9763.

[47] G. Bae, M. Chung, S. Ji, F. Jaouen, C. Choi, pH effect on the H2O2-induced deactivation of Fe-N-C catalysts, ACS Catal. 10 (2020) 8485–8495.

[48] B. Ren, H. Cui, C. Wang, Self-supported graphene nanosheet-based composites as binder-free electrodes for advanced electrochemical energy conversion and storage, Electrochem. Energy Rev. 5 (2022) 32.

[49] Y. Li, M. Gong, Y. Liang, J. Feng, J.-E. Kim, H. Wang, G. Hong, B. Zhang, H. Dai, Advanced zinc-air batteries based on high-performance hybrid electrocatalysts, Nat. Commun., 4 (2013) 1805.

[50] Z. Wang, H. Jin, T. Meng, K. Liao, W. Meng, J. Yang, D. He, Y. Xiong, S. Mu, Fe, Cu-coordinated ZIF-derived carbon framework for efficient oxygen reduction reaction and zinc–air batteries, Adv. Funct. Mater. 28 (2018) 1802596.

[51] Q. Jin, C. Wang, Y. Guo, X. Xiao, X. Tan, J. Chen, W. He, Y. Li, H. Cui, C. Wang, Axial oxygen ligands regulating electronic and geometric structure of Zn-N-C sites to boost oxygen reduction reaction, Adv. Sci. 10 (2023) 2302152.